Letter

Strong Correlation Between Superconductivity and Ferromagnetism in an Fe-Chalcogenide Superconductor

Nathan J. McLaughlin, Hailong Wang, Mengqi Huang, Eric Lee-Wong, Lunhui Hu, Hanyi Lu, Gerald Q. Yan, Genda Gu, Congjun Wu, Yi-Zhuang You, and Chunhui Rita Du*

ACCESS | Metrics & More | Article Recommendations | SI Supporting Information

ABSTRACT: The interplay among topology, superconductivity, and magnetism promises to bring a plethora of exotic and unintuitive behaviors in emergent quantum materials. The family of Fe-chalcogenide superconductors $FeTe_xSe_{1-x}$ are directly relevant in this context due to their intrinsic topological band structure, high-temperature superconductivity, and unconventional pairing symmetry. Despite enormous promise and expectation, the local magnetic properties of $FeTe_xSe_{1-x}$ remain largely unexplored, which prevents a comprehensive understanding of their underlying material properties. Exploiting nitrogen vacancy (NV) centers in diamond, here we report nanoscale quantum sensing and imaging of magnetic flux generated by exfoliated $FeTe_xSe_{1-x}$ flakes, demonstrating strong correlation between superconductivity and ferromagnetism in $FeTe_xSe_{1-x}$. The coexistence of superconductivity and ferromagnetism in an established topological superconductor opens up new opportunities for exploring exotic spin and charge transport phenomena in quantum materials. The demonstrated coupling between NV centers and $FeTe_xSe_{1-x}$ may also find applications in developing hybrid architectures for next-generation, solid-state-based quantum information technologies.

KEYWORDS: Quantum sensing, Nitrogen vacancy magnetometry, Topological superconductors, Unconventional ferromagnetism

INTRODUCTION

Topological superconductors harboring exotic Majorana Fermions have received intensive research interest over the past several years due to their significant potential for developing transformative, fault-tolerant, quantum-computing paradigms.[1,2] This emergent class of superconductors is distinguishable from its conventional counterparts by its topologically protected surface or edge state, as well as exhibiting a range of exotic and highly interesting quantum phenomena.[1,3] Among the potential material candidates, the $FeTe_xSe_{1-x}$ family naturally stands out due to its high superconducting transition temperature, simple crystal structure, and intrinsic topological band structure due to the bulk band-inversion induced by spin−orbit coupling.[4−7]

Over the past few years, pioneering research efforts have gone toward experimentally investigating the topological nature and the superconducting properties of $FeTe_xSe_{1-x}$.[4,6,8] The topological superconductivity observed in these experiments is a consequence of the proximity effect from the bulk superconductivity to the surface Dirac state. It is natural to examine whether the surface superconductivity can provide important information about the bulk gap function symmetry. In particular, time-reversal symmetry as well as parity and charge conjugation are three fundamental discrete symmetries of interest. The existence or lack of time-reversal symmetry

breaking (TRSB) is an important question for exploring pairing mechanisms in strongly correlated superconductors. TRSB pairing symmetries have been theoretically proposed in iron-based superconductors.[9] Experimentally, thermal transport and angle-resolved photoemission spectroscopy studies suggest the spontaneous TRSB and opening of a band gap at the surface Dirac cone in superconducting $FeTe_xSe_{1-x}$,[10,11] which indicates the presence of ferromagnetism induced by an intrinsic unconventional pairing symmetry.[12] The interplay among topology,[4,6,8,13] superconductivity,[4,7] and magnetism[10,11] makes $FeTe_xSe_{1-x}$ an attractive platform to explore a range of emergent quantum spin and charge transport phenomena,[11,14,15] such as Majorana Fermions[6,8] and higher-order topological superconductivity[16−18] as recently reported. Despite remarkable progress, detailed knowledge of the local magnetic properties of superconducting $FeTe_xSe_{1-x}$ remains elusive, and direct evidence to corroborate the coexistence of superconductivity and ferromagnetism in $FeTe_xSe_{1-x}$ is still
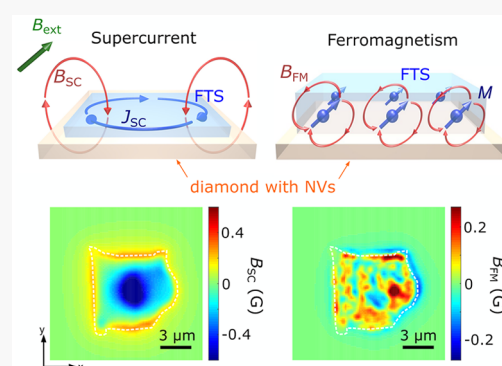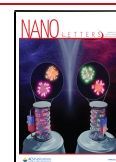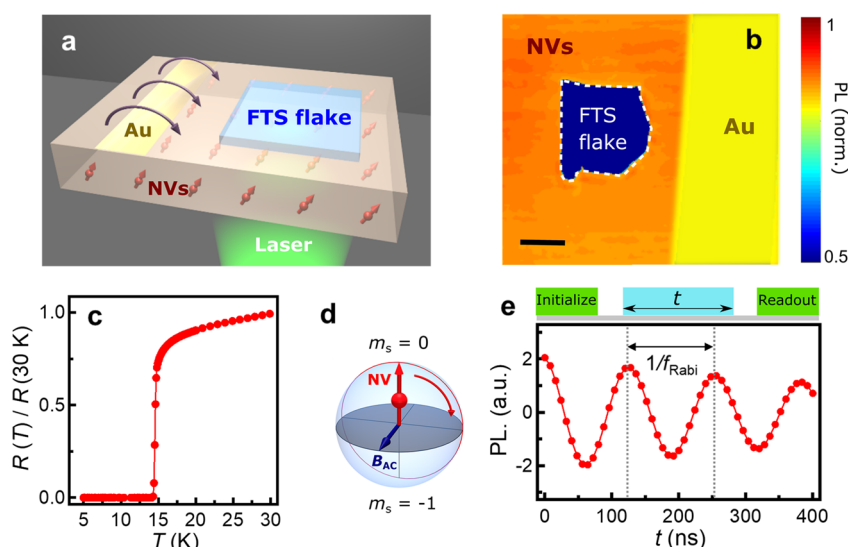
Figure 1. Measurement of magnetic flux generated by an exfoliated FTS flake by NV centers. (a) Schematic of an exfoliated FTS flake transferred onto a diamond membrane for NV wide-field magnetic imaging measurements. (b) Photoluminescence image showing an overview of a prepared NV-FTS device. The scale bar is 5 μm. (c) Electrical transport measurements show a characteristic superconducting phase transition at 14.5 K for an exfoliated FTS flake. (d,e) Schematic of Rabi oscillations on the Bloch sphere and an experimental measurement spectrum of NV Rabi oscillation. The top panel of (e) shows the optical and microwave sequence of NV Rabi oscillation measurements.

lacking. The major difficulty results from the fact that the magnetic flux generated by superconductors is often shielded by the Meissner effect,[19] which is challenging to access using conventional magnetometry methods.

Here, we introduce nitrogen-vacancy (NV) centers,[20,21] optically active atomic defects in diamond that act as single-spin sensors, to perform nanoscale quantum imaging and sensing of magnetic flux generated by an exfoliated $FeTe_{0.7}Se_{0.3}$ (FTS) flake.[11] By performing NV Rabi oscillation measurements,[22,23] we directly image the spatial distribution of supercurrents in FTS. By measuring magnetic stray fields and fluctuations by the NV optical detection of magnetic resonance (ODMR) and relaxometry techniques,[24−28] we demonstrate strong correlation between superconductivity and ferromagnetism in FTS.[12] The presented NV quantum sensing and imaging platform operates in an accessible, table-top format, which can be extended naturally to a large family of two-dimensional van der Waals materials,[29] providing new opportunities for investigating local electrical and magnetic behaviors in emergent quantum materials.

EXPERIMENTAL DETAILS

Figure 1a shows a schematic of our measurement platform, where a 140 nm thick FTS flake with lateral dimensions of ~11 μm × ~9 μm is transferred onto a single crystal diamond substrate containing NV centers implanted ~5 nm below the surface. The density of NV centers is characterized to be ~1500/μm^2, providing a convenient platform to achieve wide-field imaging based on the ensemble of NV spins.[30−32] An on-chip Au stripline is fabricated on the diamond sample, allowing the application of microwave currents to control the quantum spin state of the NV centers. A photoluminescence image [Figure 1b] shows an overview of a prepared NV-FTS device, where an FTS flake is located ~4 μm from the Au stripline. The exfoliated FTS flake exhibits the characteristic super-conducting phase transition at T_c = 14.5 K, as shown in Figure 1c, in agreement with the previous electrical transport study (see Supporting Information Section 1 for details).[10]

We first employed NV wide-field microscopy[30−32] to perform Rabi oscillation measurements to image circular AC supercurrents in the FTS flake. An NV center is formed by a nitrogen atom adjacent to a carbon atom vacancy in one of the nearest neighboring sites of a diamond crystal lattice.[21] The negatively charged NV state has an S = 1 electron spin and serves as a three-level quantum system. When a microwave magnetic field at the electron spin resonance (ESR) frequency is applied to the NV site, the NV spin will oscillate periodically between two different states, for example, those with m_s = 0 and m_s = −1 in the Bloch sphere, as illustrated in Figure 1d. These are referred to as Rabi oscillations.[23,33] Because the m_s = ±1 spin states of NV centers are more likely to be trapped by a nonradiative pathway back to the m_s = 0 ground state and emit reduced photoluminescence,[21] Rabi oscillations of the NV spin can be optically accessed by measuring the spin-dependent photoluminescence. The top panel of Figure 1e shows the optical and microwave sequence for Rabi oscillation measurements by an NV wide-field microscopy. A 1 μs long green laser pulse is first applied to initialize the NV spin to the m_s = 0 state. A microwave pulse at the NV ESR frequency is applied to induce the NV spin transition followed by a second green laser pulse to measure the spin-dependent photoluminescence of NV centers and to reinitialize the NV spins for the next measurement sequence. The microwave pulse is applied 700 ns after turning off the initialization green laser pulse to minimize the laser-induced heating and electric/magnetic excitations. The entire measurement sequence is repeated 15 000 times during one camera exposure period and the duration of the microwave pulse systematically varies from zero to a few hundred nanoseconds at different camera exposure periods in order to detect a time-dependent variation of NV photo-luminescence. The bottom panel of Figure 1e shows a characteristic NV Rabi oscillation spectrum. The amplitude of the applied microwave magnetic field B_{AC} can be obtained by the frequency of the Rabi oscillation f_{Rabi} as follows: B_{AC} =

$\frac{\sqrt{3}f_{Rabi}}{\gamma}$, where γ is the gyromagnetic ratio of an NV spin (see Supporting Information Section 2 for details).

In the prepared NV-FTS device, the microwave magnetic field B_{AC} at individual NV sites contains two potential contributions: the oscillating Oersted field B_{MW} produced by the microwave current flowing in the on-chip Au stripline and the magnetic field B_{SU} generated by supercurrents in the FTS flake, as illustrated in Figure 2a,b. When $T > T_c$, the Rabi
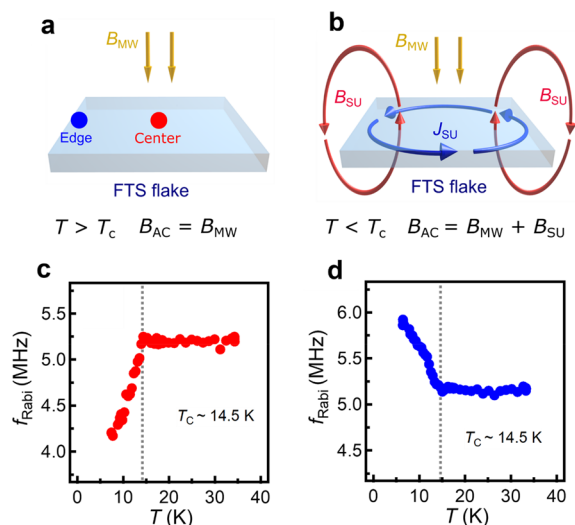
Figure 2. Local quantum sensing of superconducting phase transition of an FTS flake. (a,b) Schematic of the spatial profile of the microwave magnetic field environment of an FTS flake above and below T_c. (c), (d) Temperature dependence of Rabi oscillation frequency f_{Rabi} of NV centers located underneath the central (c) and edge (d) areas of the FTS flake. The Meissner screening effect reduces (increases) the effective microwave field in the central (edge) area of the FTS flake, leading to the opposite variations of f_{Rabi} across T_c.

oscillation of NV centers is only driven by the Oersted field B_{MW}. When temperature falls below T_c, circular supercurrents in FTS modify the spatial distribution of the microwave magnetic field surrounding the FTS flake. In the central area of the FTS flake, the microwave field B_{SU} generated by supercurrents is in the opposite direction of the external microwave field B_{MW}, effectively reducing the NV Rabi oscillation rate f_{Rabi}. B_{SU} and B_{MW} follow the same direction in the boundary area of the FTS flake, leading to an enhancement of f_{Rabi}. Figure 2c,d shows the temperature dependence of the measured Rabi oscillation frequency f_{Rabi} for NV centers underneath the central and boundary areas of the FTS flake, respectively. Notably, f_{Rabi} exhibits a sudden decrease (increase) when temperature falls below the T_c of FTS, in agreement with the picture of the Meissner screening effect discussed above.[33,34] By subtracting the external microwave field generated by the on-chip Au stripline, the internal magnetic field B_{SU} due exclusively to the circulating supercurrents in the FTS flake can be extracted (see Supporting Information Section 2 for details).

Figure 3a−c shows 2D maps of B_{SU} measured at 5, 8.5, and 10 K. When $T = 5$ K, magnetic flux expulsion due to the Meissner effect[34,35] leads to a negative magnetic field in the central area of the flake and a positive magnetic field in the edge area. Note that the sign of B_{SU} represents its orientation

relative to the external microwave field. The magnitude of B_{SU} decreases with increasing temperature and eventually vanishes above T_c. Without considering the variation along the thickness direction, the spatially resolved B_{SU} allows us to reconstruct the 2D distribution of supercurrent J_{SU} in the FTS flake, as shown in Figure 3d−f (see Supporting Information Section 3 for details).[30,31] The supercurrent forms a circular loop with a maximum density of ~1 mA/μm². It gradually decays and approaches zero in the central region of the FTS flake. The length scale that the supercurrents decay inside a superconductor is determined by the London penetration depth λ.[33] Microscopically, λ is associated with the imaginary part of the electrical conductivity and the superfluid density of FTS.[33] Using a machine learning analysis model,[36] we fit the spatial distribution of the microwave field B_{SU} to obtain 2D maps of London penetration depth, as shown in Figure 3g−i (see Supporting Information Section 4 for details). The spatial variation of λ within the exfoliated FTS flake demonstrates the existence of superconducting domains possibly induced by inhomogeneities or defects.[6]

In conventional s-wave superconductors, ferromagnetism is usually prohibited because the characteristic spin-singlet s-wave pairing rule dictates antiparallel spin configuration of cooper pairs. Thus, the emergence of superconductivity-induced ferromagnetism is usually accompanied by the spin triplet states or unconventional superconducting pairing symmetries such as experimentally observed in UPt$_3$,[37] UTe$_2$,[38] Ba$_{1−x}$K$_x$Fe$_2$As$_2$,[39] and recently theoretically predicted in FTS.[12] Next, we employ the NV ODMR technique[40−42] to detect magnetic stray fields generated by a superconducting FTS flake, providing direct evidence to the superconductivity-correlated ferromagnetism. Figure 4a shows a schematic of our measurement geometry. An external magnetic field $B_{ext} \sim 60$ G is applied with an angle of 39° relative to the normal of the sample plane. The in-plane projection of B_{ext} is approximately along the x-axis direction. Note that both supercurrents and magnetization in the FTS flake can potentially produce a sizable stray field. If the superconductivity-correlated ferromagnetism is spontaneously aligned to the direction of the external magnetic field, the out-of-plane component of the stray field generated by a tilted ferro-magnetization is negligibly small in the central area of the FTS flake and exhibits opposite signs at the $+x$ and $−x$ boundaries, as illustrated in Figure 4a. In contrast, the out-of-plane component of the internal field generated by supercurrents follows the characteristic Meissner effect, exhibiting a decrease in the center and an increase on the boundary of the FTS flake, as shown in Figure 2b. On the basis of these two distinct spatial geometries, we can qualitatively separate these two effects.

The top panel of Figure 4b shows the microwave and optical sequence of pulsed NV ODMR measurements. We utilize 1 μs long green laser pulses for NV initialization and readout and 100 ns long microwave π-pulses to induce NV spin transitions. The entire sequence is repeated 15 000 times during one camera exposure period and the frequency f of the microwave pulses is swept for different camera exposure periods. When f matches the NV ESR conditions, reduced photoluminescence is observed. Note that the NV ensemble used in our study has four pairs of ESR transitions in one ODMR spectrum in response to an arbitrary magnetic field, allowing extraction of the out-of-plane component of the internal stray field B_z generated by the FTS flake (see Supporting Information Section 5 for details). Figure 4b,f shows the 2D maps of B_z
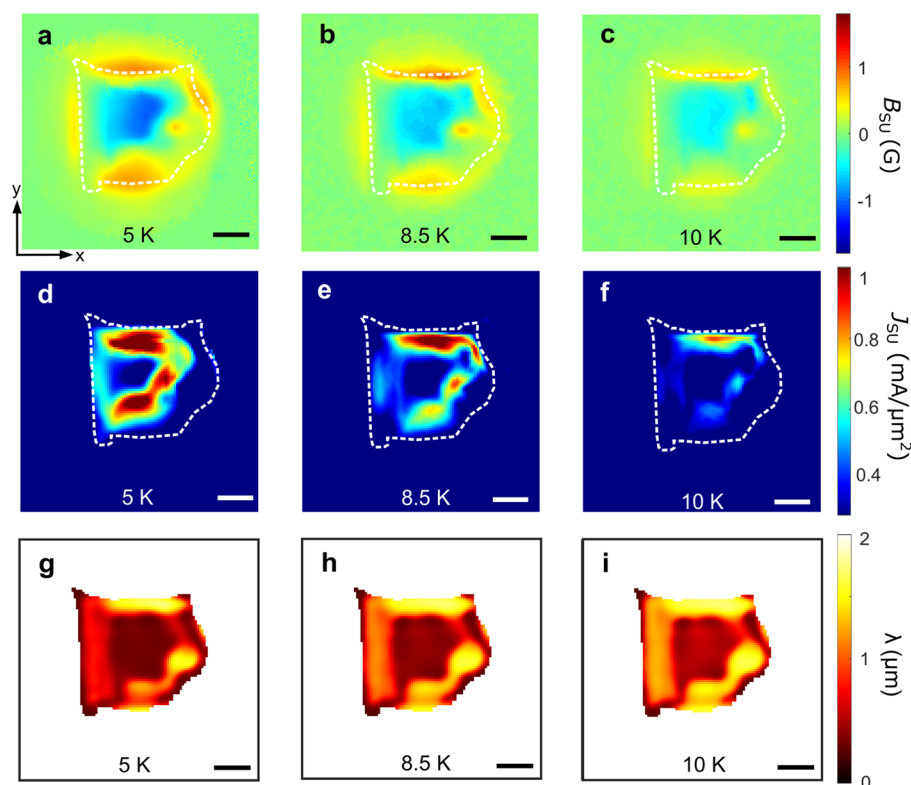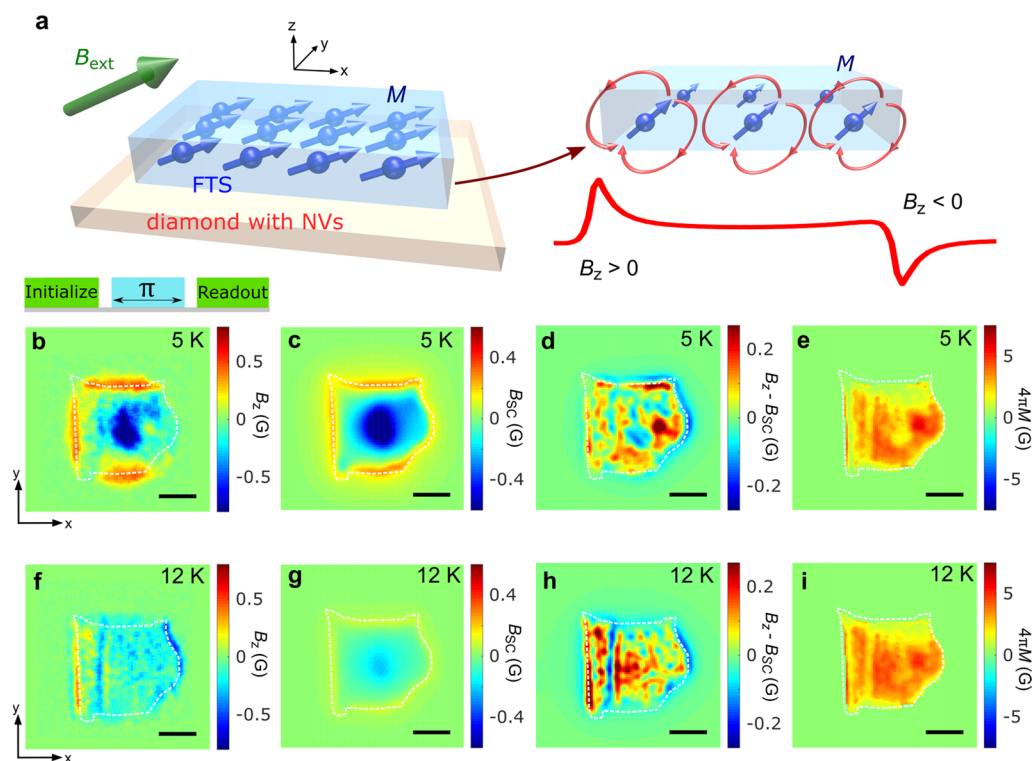
Figure 3. NV wide-field imaging of the internal microwave magnetic field, supercurrents, and London penetration depth of an FTS flake. (a−c) Two-dimensional imaging of the internal microwave magnetic field B_{SU} generated by supercurrents in the FTS flake at 5, 8.5, and 12 K. (d−f) Reconstructed spatial distribution of supercurrents in the FTS flake at 5, 8.5, and 12 K. (g−i) Two-dimensional maps of London penetration depth λ reconstructed by machining learning analysis with an assumption of a spatially dependent microwave conductivity. For all panels, the white dashed line marks the boundary of the exfoliated FTS flake and scale bar is 3 μm.

measured at 5 and 12 K, respectively. When $T < T_c$, $B_z = B_{SC} + B_{FM}$, where B_{SC} and B_{FM} represent the out-of-plane static magnetic fields produced by supercurrents and ferromagnetism in the FTS flake, respectively. At 5 K, B_z is dominated by the Meissner screening effect, showing a positive value at the boundary area of the FTS flake and a negative value in the central region. While the contribution of B_{FM} is heavily masked in this situation, the asymmetry of B_z along the x-axis direction indicates the existence of a tilted magnetization in the FTS flake. When $T = 12$ K in proximity to T_c, the Meissner effect is significantly suppressed due to the reduced supercurrents, thus, the asymmetry of B_z becomes more pronounced. The sign of B_z reverses at the two opposite boundaries of the FTS flake, providing clear evidence to the induced magnetic moment in superconducting FTS.

To quantitatively separate the two mutually entangled effects, we performed machine-learning assisted simulations to reconstruct the spatially dependent magnetic field B_{SC} and B_{FM}. In brief, we first fit the measured B_z using the model of the Meissner effect to get the stray field B_{SC} produced by supercurrents. The remaining part $(B_z - B_{SC})$ will be fitted to the expression of the stray field B_{FM} produced by the superconductivity-correlated ferromagnetism in FTS (see Supporting Information Section 6 for details). Figure 4c,d,g,h shows the extracted 2D maps of B_{SC} and $(B_z - B_{SC})$ at 5 and 12 K, respectively. The contribution from the supercurrents (Figures 4c,g) largely resembles the Meissner effect and becomes significantly reduced when temperature approaches T_c. The obtained 2D map of $(B_z - B_{SC})$ follows the "sign reversal" feature at the $+x$ and $-x$ boundaries of the FTS flake,

suggesting that the induced magnetic moment follows the direction of the external magnetic field. Note that the screening effect of in-plane magnetic fields by the supercurrents could also lead to an asymmetric magnetic field profile, however, with an opposite sign to a ferromagnet. Thus, such an effect does not play a significant role in our experiments (see Supporting Information Section 6 for details). It is worth mentioning that $(B_z - B_{SC})$ exhibits a nonuniform distribution, indicating a multidomain structure [Figure 4d,h] of the superconductivity-correlated ferromagnetism in the FTS flake, which can be attributable to defects, inhomogeneity, and domain wall pinning effects.[42] When the in-plane component of the external magnetic field B_{ext} is rotated by ∼130°, the observed B_{SC} largely remains the same while the field pattern of $(B_z - B_{SC})$ rotates accordingly (see Supporting Information Section 6 for details), confirming the weak anisotropy of the superconductivity-correlated ferromagnetism whose orientation is tunable by the external magnetic field. On the basis of the spatial-dependent $(B_z - B_{SC})$, we further reconstructed the 2D profile of the magnetization $4\pi M$ of FTS, as shown in Figure 4e,i (see Supporting Information Section 6 for details). The obtained $4\pi M$ exhibits spatially dependent variation with an average value of ∼4 G for $T < T_c$. Theoretically, the upper limit of M of superconducting FTS can be estimated by assuming that all the charge carriers are polarized: $M_{max} = \frac{b\mu_B}{V}$, where $b\mu_B$ is the magnetization of each Fe atom, μ_B is the Bohr magneton, and V is the average volume containing one Fe cation. With $b = 0.0464$ and $V = 1.0 \times 10^{-28}$ m³,[12] $4\pi M_{max}$ is calculated to be 15 Oe, which is in qualitative

Figure 4. NV wide-field imaging of superconductivity-correlated ferromagnetism in FTS. (a) Experimental measurement geometry to detect superconductivity-correlated ferromagnetism in an FTS flake. An external magnetic field B_{ext} is applied to tilt the magnetization away from the equilibrium position (out-of-plane direction, z-axis). The in-plane projection of B_{ext} is approximately along the x-axis direction. The out-of-plane component of the internal DC magnetic field generated by the ferromagnetism shows the sign reversal feature at the $+x$ and $-x$ boundaries of the FTS flake. (b,f) Two-dimensional wide-field imaging of internal magnetic field B_z generated by the FTS flake at 5 K (b) and 12 K (f). (Top panel of b) Optical and microwave sequence of NV ODMR measurements. (c,g) Extracted 2D images of stray field B_{SC} produced by supercurrents at 5 K (c) and 12 K (g). (d,h) Extracted 2D images of stray field $(B_z - B_{SC})$ generated by the superconductivity-correlated ferromagnetism at 5 K (d) and 12 K (h). (e,i) Reconstructed spatially dependent magnetization of the superconducting FTS flake at 5 K (e) and 12 K (i). For panels (b−i), the white dashed line marks the boundary of the exfoliated FTS flake and scale bar is 3 μm.

agreement with our experimental results. We highlight that the measured spin susceptibility of FTS at 12 K is about 200 times larger than the value measured in the paramagnetic state (see Supporting Information Section 1 for details), suggesting that the observed magnetic moment cannot be a result of spin polarization induced by the external magnetic field. In addition, we also performed NV measurements of the stray field B_z produced by FTS above T_c. The measured magnetic field falls below our detection limit over entire measurement region at 16 K (see Supporting Information Section 6 for details). All of these results demonstrate that the observed ferromagnetism is indeed driven by the superconductivity in FTS. In addition to DC stray fields, the superconductivity-correlated ferromagnetism in FTS also generates fluctuating magnetic fields at the characteristic frequencies of thermal magnons. When the frequency of FTS magnons matches the NV ESR frequency, the magnetic fluctuations will induce spin transitions of a proximal NV center. Our experimentally measured NV relaxometry results are well correlated to the field-dependent variation of the magnon density of FTS, providing another piece of evidence to the ferromagnetism in superconducting FTS (see Supporting Information Section 7 for details).[24,43]

Next, we briefly discuss the physical origin of the observed strong correlation between superconductivity and ferromagnetism. In FTS, the superconducting carriers are electrons and holes near the Fermi level, and localized magnetic moments can be carried by the d orbitals of Fe atoms,[44] impurities, or defects. Because of the weak exchange coupling of carriers at the Fe sites, long-range ferromagnetic ordering is absent in the normal state. When $T < T_c$, TRSB accompanied by unconventional pairing symmetries could take place, leading to the emergence of ferromagnetism in FTS. Because of the multiorbital nature of the Fe atoms,[12] there may exist nearly degenerate gap function symmetries. To reduce the free energy, they often prefer a superposition with a relative $\pm\frac{\pi}{2}$ phase difference in the mean-field theory. The ferromagnetic order is inversion symmetric, hence, it can only be induced by mixing two pairing orders with the same parity. The mixing between A_{1g} and A_{2g} or B_{1g} and B_{2g} can yield the ferromagnetic order along the z-direction. On the other hand, the in-plane component of ferromagnetism could be a consequence of mixing a pairing symmetry of A or B-type with a two-dimensional representation of the E-type.[12] Loosely speaking, A, B, and E refer to the s, d and p-wave pairing symmetries respectively; the subindices 1 and 2 refer to the parity with respect to the vertical plane reflection; and g means even parity under inversion. Because of the orbital degree of freedom, the E-type pairing symmetry can also be spin-singlet. Such a complex pairing gap function can couple to the bulk magnetization via spin−orbit coupling according to a symmetry analysis,[12] enabling the establishment of a long-range magnetic order in superconducting FTS. This driving force is due to the TRSB Cooper pairing, whose effect may be

weak. Nevertheless, the FTS system contains local moments,[44] and they may be further aligned by the bulk magnetization to amplify such effect.

In summary, we have demonstrated NV-based quantum sensing and imaging of magnetic flux generated by exfoliated FTS flakes. The obtained spatial profile of stray fields generated by supercurrents in FTS flakes follows the characteristic Meissner screening effect. By employing NV ODMR method, we provide direct evidence of super-conductivity-correlated ferromagnetism in FTS, opening up new opportunities for exploring the rich physics related to the interplay among topology, superconductivity, and magnetism in topological superconductors. At the same time, our results also reveal the unconventional pairing mechanism and the time reversal symmetry breaking in FTS, demonstrating NV centers as a versatile local probe to investigate nanoscale electrical and magnetic properties of emergent quantum materials. The observed spatially tunable coupling between NV centers and superconducting FTS also provides a new route for developing hybrid quantum architectures,[45] aiding in the development of next-generation, solid-state-based quantum information technologies.

■ ASSOCIATED CONTENT

Ⓢ Supporting Information

The Supporting Information is available free of charge at https://pubs.acs.org/doi/10.1021/acs.nanolett.1c02424.

> Details on materials and methods; numerical analysis of NV results to extract stray fields, supercurrents, ferromagnetism, and London penetration depth; NV relaxometry measurement results (PDF)

■ AUTHOR INFORMATION

Corresponding Author

Chunhui Rita Du − *Department of Physics and Center for Memory and Recording Research, University of California, San Diego, La Jolla, California 92093, United States;* ⓞ orcid.org/0000-0001-8063-7711; Email: c1du@physics.ucsd.edu

Authors

Nathan J. McLaughlin − *Department of Physics, University of California, San Diego, La Jolla, California 92093, United States*

Hailong Wang − *Center for Memory and Recording Research, University of California, San Diego, La Jolla, California 92093, United States*

Mengqi Huang − *Department of Physics, University of California, San Diego, La Jolla, California 92093, United States*

Eric Lee-Wong − *Department of Physics and Department of NanoEngineering, University of California, San Diego, La Jolla, California 92093, United States*

Lunhui Hu − *Department of Physics, University of California, San Diego, La Jolla, California 92093, United States*

Hanyi Lu − *Department of Physics, University of California, San Diego, La Jolla, California 92093, United States*

Gerald Q. Yan − *Department of Physics, University of California, San Diego, La Jolla, California 92093, United States*

Genda Gu − *Condensed Matter Physics and Materials Science Division, Brookhaven National Laboratory, Upton, New York 11973, United States*

Congjun Wu − *Department of Physics, University of California, San Diego, La Jolla, California 92093, United States; School of Science, Westlake University, Hangzhou, Zhejiang 310024, China; Institute of Natural Sciences, Westlake Institute for Advanced Study, Hangzhou, Zhejiang 310024, China*

Yi-Zhuang You − *Department of Physics, University of California, San Diego, La Jolla, California 92093, United States*

Complete contact information is available at:
https://pubs.acs.org/10.1021/acs.nanolett.1c02424

Author Contributions

N.M. performed the measurements and analyzed the data with help from H.W., M.H., G.Q.Y., and H.L. E.L.-W. built the optical setup and prepared the device. G.G. provided the FTS crystals. L.H., C.W., and Y.-Z.Y. provided theoretical guidance. H.W. and C.H.R.D. wrote the manuscript with the help from all coauthors. C.H.R.D. supervised this project.

Notes

The authors declare no competing financial interest.

■ ACKNOWLEDGMENTS

■ REFERENCES

(1) Qi, X. L.; Zhang, S. C. Topological insulators and super-conductors. *Rev. Mod. Phys.* **2011**, *83*, 1057.

(2) Nayak, C.; Simon, S. H.; Stern, A.; Freedman, M.; Das Sarma, S. Non-Abelian anyons and topological quantum computation. *Rev. Mod. Phys.* **2008**, *80*, 1083.

(3) Frolov, S. M.; Manfra, M. J.; Sau, J. D. Topological superconductivity in hybrid devices. *Nat. Phys.* **2020**, *16*, 718.

(4) Zhang, P.; et al. Observation of topological superconductivity on the surface of an iron-based superconductor. *Science* **2018**, *360*, 182.

(5) Johnson, P. D.; et al. Spin-orbit interactions and the nematicity observed in the Fe-based superconductors. *Phys. Rev. Lett.* **2015**, *114*, 167001.

(6) Wang, Z.; et al. Evidence for dispersing 1D Majorana channels in an iron-based superconductor. *Science* **2020**, *367*, 104.

(7) Li, Y.; et al. Electronic properties of the bulk and surface states of $Fe_{1+y}Te_{1-x}Se_x$. *Nat. Mater.* **2021**; DOI: 10.1038/s41563-021-00984-7.

(8) Wang, D.; et al. Evidence for Majorana bound states in an iron-based superconductor. *Science* **2018**, *362*, 333.

(9) Lee, W. C.; Zhang, S. C.; Wu, C. Pairing state with a time-reversal symmetry breaking in FeAs-based superconductors. *Phys. Rev. Lett.* **2009**, *102*, 217002.

(10) Chen, L.; et al. Spontaneous Nernst effect in the iron-based superconductor $Fe_{1+y}Te_{1-x}Se_x$. *Phys. Rev. B: Condens. Matter Mater. Phys.* **2020**, *102*, 054503.

(11) Zaki, N.; Gu, G.; Tsvelik, A. M.; Wu, C.; Johnson, P. D. Time reversal symmetry breaking in the Fe-chalcogenide superconductors. *Proc. Natl. Acad. Sci. U. S. A.* **2021**, *118*, e2007241118.

(12) Hu, L.-H.; Johnson, P. D.; Wu, C. Pairing symmetry and topological surface state in iron-chalcogenide superconductors. *Phys. Rev. Res.* **2020**, *2*, 022021.

(13) Rameau, J. D.; Zaki, N.; Gu, G. D.; Johnson, P. D.; Weinert, M. Interplay of paramagnetism and topology in the Fe-chalcogenide high-T_c superconductors. *Phys. Rev. B: Condens. Matter Mater. Phys.* **2019**, *99*, 205117.

(14) Ge, Z.; et al. Superconductivity on edge: evidence of a one-dimensional superconducting channel at the edges of single-layer FeTeSe antiferromagnetic nanoribbons. *ACS Nano* **2020**, *14*, 6539.

(15) Jiang, D.; et al. Observation of robust edge superconductivity in Fe(Se,Te) under strong magnetic perturbation. *Sci. Bull.* **2021**, *66*, 425.

(16) Gray, M. J.; et al. Evidence for helical hinge zero modes in an Fe-based superconductor. *Nano Lett.* **2019**, *19*, 4890.

(17) Zhang, R.-X.; Cole, W. S.; Das Sarma, S. Helical hinge Majorana modes in iron-based superconductors. *Phys. Rev. Lett.* **2019**, *122*, 187001.

(18) Zhang, R.-X.; Cole, W. S.; Wu, X.; Das Sarma, S. Higher-order topology and nodal topological superconductivity in Fe(Se,Te) heterostructures. *Phys. Rev. Lett.* **2019**, *123*, 167001.

(19) Meissner, W.; Ochsenfeld, R. Ein neuer Effekt bei Eintritt der Supraleitfähigkeit. *Naturwissenschaften* **1933**, *21*, 787.

(20) Degen, C. L.; Reinhard, F.; Cappellaro, P. Quantum sensing. *Rev. Mod. Phys.* **2017**, *89*, 035002.

(21) Rondin, L.; et al. Magnetometry with nitrogen-vacancy defects in diamond. *Rep. Prog. Phys.* **2014**, *77*, 056503.

(22) Jelezko, F.; Gaebel, T.; Popa, I.; Gruber, A.; Wrachtrup, J. Observation of coherent oscillations in a single electron spin. *Phys. Rev. Lett.* **2004**, *92*, 076401.

(23) Fuchs, G. D.; Dobrovitski, V. V.; Toyli, D. M.; Heremans, F. J.; Awschalom, D. D. Gigahertz dynamics of a strongly driven single quantum spin. *Science* **2009**, *326*, 1520.

(24) Du, C.; et al. Control and local measurement of the spin chemical potential in a magnetic insulator. *Science* **2017**, *357*, 195.

(25) McCullian, B. A.; Thabt, A. M.; Gray, B. A.; Melendez, A. L.; Wolf, M. S.; Safonov, V. L.; Pelekhov, D. V.; Bhallamudi, V. P.; Page, M. R.; Hammel, P. C. Broadband multi-magnon relaxometry using a quantum spin sensor for high frequency ferromagnetic dynamics sensing. *Nat. Commun.* **2020**, *11*, 5229.

(26) Kolkowitz, S.; et al. Probing Johnson noise and ballistic transport in normal metals with a single-spin qubit. *Science* **2015**, *347*, 1129.

(27) Finco, A.; Haykal, A.; Tanos, R.; Fabre, F.; Chouaieb, S.; Akhtar, W.; Robert-Philip, I.; Legrand, W.; Ajejas, F.; Bouzehouane, K.; Reyren, N.; Devolder, T.; Adam, J.-P.; Kim, J.-V.; Cros, V.; Jacques, V. Imaging non-collinear antiferromagnetic textures via single spin relaxometry. *Nat. Commun.* **2021**, *12*, 767.

(28) Andersen, T. I.; et al. Electron-phonon instability in graphene revealed by global and local noise probes. *Science* **2019**, *364*, 154.

(29) Geim, A. K.; Grigorieva, I. V. Van der Waals heterostructures. *Nature* **2013**, *499*, 419.

(30) Tetienne, J. P.; et al. Quantum imaging of current flow in graphene. *Sci. Adv.* **2017**, *3*, e1602429.

(31) Ku, M. J. H.; et al. Imaging viscous flow of the Dirac fluid in graphene. *Nature* **2020**, *583*, 537.

(32) Lenz, T.; et al. Imaging topological spin structures using light-polarization and magnetic microscopy. *Phys. Rev. Appl.* **2021**, *15*, 024040.

(33) Xu, Y.; et al. Mapping dynamical magnetic responses of ultrathin micron-size superconducting films using nitrogen-vacancy centers in diamond. *Nano Lett.* **2019**, *19*, 5697.

(34) Nusran, N. M.; et al. Spatially-resolved study of the Meissner effect in superconductors using NV-centers-in-diamond optical magnetometry. *New J. Phys.* **2018**, *20*, 043010.

(35) Rohner, D.; et al. Real-space probing of the local magnetic response of thin-film superconductors using single spin magnetometry. *Sensors* **2018**, *18*, 3790.

(36) Paszke, A.; et al. PyTorch: An imperative style, high-performance deep learning library. *Advances in Neural Information Processing Systems* **2019**, *32*, 8024.

(37) Luke, G. M.; et al. Muon spin relaxation in UPt$_3$. *Phys. Rev. Lett.* **1993**, *71*, 1466.

(38) Jiao, L.; et al. Chiral superconductivity in heavy-fermion metal UTe$_2$. *Nature* **2020**, *579*, 523.

(39) Grinenko, V.; et al. Superconductivity with broken time-reversal symmetry inside a superconducting *s*-wave state. *Nat. Phys.* **2020**, *16*, 789.

(40) Pelliccione, M.; et al. Scanned probe imaging of nanoscale magnetism at cryogenic temperatures with a single-spin quantum sensor. *Nat. Nanotechnol.* **2016**, *11*, 700.

(41) Thiel, L.; et al. Probing magnetism in 2D materials at the nanoscale with single-spin microscopy. *Science* **2019**, *364*, 973.

(42) Sun, Q.-C.; Song, T.; Anderson, E.; Brunner, A.; Forster, J.; Shalomayeva, T.; Taniguchi, T.; Watanabe, K.; Grafe, J.; Stohr, R.; Xu, X.; Wrachtrup, J. Magnetic domains and domain wall pinning in two-dimensional ferromagnets revealed by nanoscale imaging. *Nat. Commun.* **2021**, *12*, 1989.

(43) van der Sar, T.; Casola, F.; Walsworth, R.; Yacoby, A. Nanometre-scale probing of spin waves using single-electron spins. *Nat. Commun.* **2015**, *6*, 7886.

(44) You, Y. Z.; Yang, F.; Kou, S. P.; Weng, Z. Y. Magnetic and superconducting instabilities in a hybrid model of itinerant/localized electrons for iron pnictides. *Phys. Rev. B: Condens. Matter Mater. Phys.* **2011**, *84*, 054527.

(45) Wang, X.; Xiao, Y.; Liu, C.; Lee-Wong, E.; McLaughlin, N. J.; Wang, H.; Wu, M.; Wang, H.; Fullerton, E. E.; Du, C. R. Electrical control of coherent spin rotation of a single-spin qubit. *npj Quantum Inf.* **2020**, *6*, 78.

■ NOTE ADDED AFTER ASAP PUBLICATION

This paper was originally published ASAP on August 20, 2021, with an error in the Supporting Information. The corrected version was posted on August 23, 2021.